Delft University of Technology

# Three-dimensional flows in the wake of a non-cavitating and cavitating marine propeller

Başkan Perçin, Özge; Fiscaletti, Daniele; Elsinga, Gerrit E.; van Terwisga, Tom

**DOI**
10.1007/s00348-024-03888-9

**Publication date**
2024

**Document Version**
Final published version

**Published in**
Experiments in Fluids

**Citation (APA)**
Başkan Perçin, Ö., Fiscaletti, D., Elsinga, G. E., & van Terwisga, T. (2024). Three-dimensional flows in the wake of a non-cavitating and cavitating marine propeller. *Experiments in Fluids*, *65*(10), Article 149. https://doi.org/10.1007/s00348-024-03888-9

**Important note**
To cite this publication, please use the final published version (if applicable). Please check the document version above.

**Copyright**
Other than for strictly personal use, it is not permitted to download, forward or distribute the text or part of it, without the consent of the author(s) and/or copyright holder(s), unless the work is under an open content license such as Creative Commons.

**Takedown policy**
Please contact us and provide details if you believe this document breaches copyrights. We will remove access to the work immediately and investigate your claim.

*This work is downloaded from Delft University of Technology.*
*For technical reasons the number of authors shown on this cover page is limited to a maximum of 10.*

***Green Open Access added to TU Delft Institutional Repository***

***'You share, we take care!' - Taverne project***

***https://www.openaccess.nl/en/you-share-we-take-care***

Otherwise as indicated in the copyright section: the publisher
is the copyright holder of this work and the author uses the
Dutch legislation to make this work public.

Experiments in Fluids (2024) 65:149
https://doi.org/10.1007/s00348-024-03888-9

RESEARCH ARTICLE

# Three-dimensional flows in the wake of a non-cavitating and cavitating marine propeller

Özge Başkan Perçin[1] · Daniele Fiscaletti[2] · Gerrit E. Elsinga[3] · Tom van Terwisga[2]

Received: 25 April 2024 / Revised: 13 September 2024 / Accepted: 14 September 2024
© The Author(s), under exclusive licence to Springer-Verlag GmbH Germany, part of Springer Nature 2024

## Abstract

Tip-vortex cavitation is among the first forms of cavitation to appear around ship propellers. In the present study, the time-resolved three-dimensional flow field around non-cavitating and cavitating tip vortices in the wake of a marine propeller is investigated with tomographic PIV. The advance ratio of the propeller and the Reynolds number of the flow are kept constant, while the cavitation number is varied by changing the pressure inside the cavitation tunnel. The importance of masking the tip-vortex cavities before performing the tomographic reconstruction is firstly demonstrated, followed by a description of the applied masking algorithm. From the three-dimensional velocity vector fields, coherent structures of vorticity are identified using the $Q$-criterion. Three types of coherent structures are observed to populate the wake of the propeller, i.e. tip vortex, hub vortex, and secondary vortical structures. The secondary vortical structures surrounding the tip vortex appear to be progressively smaller in size and more chaotically-organized for decreasing cavitation number. This can be attributed to the pressure fluctuations induced by the cavity, which strengthen when the cavity size grows.

## 1 Introduction

In water, a liquid-to-gas transition occurs when locally the pressure of the water falls below a critical pressure, often assumed to be the vapour pressure. The phenomenon generating the described phase transition is known as cavitation, and it determines the sudden formation of vapour-filled cavities of variable size (multiphase flow). Cavitation occurs in several processes of engineering relevance, from turbomachines to mechanical heart valves, from ultrasonic cleaning to ship propellers (Arndt 1981).

Tip-vortex cavitation is among the first forms of cavitation to appear in ship propellers (Carlton 2018). A tip vortex arises at the tip of a propeller blade as a result of the pressure difference between the suction and the pressure sides. Tip-vortex cavitation is particularly undesirable in marine propellers. Besides causing erosion to the tip of the propeller blade, it is an important contributor to shipping noise (Carlton 2018), and it produces hull vibrations leading to passengers' discomfort (Bosschers 2018b). Recent studies evidenced that shipping noise detrimentally affects marine animals by disrupting their vital behaviours, such as foraging and resting (Hildebrand 2009; IMO 2014). An impact on their reproductive activity was reported, too, with severe implications for their demography (Jones 2009; Duarte et al. 2021). A strategy to delay cavitation and to reduce the size of tip vortex cavities is to mitigate the vortex strength by unloading the blade tip. Also, increasing the propeller clearance would considerably attenuate the hull-pressure fluctuations. However, both unloading the tip blade and increasing the propeller clearance would penalize the propulsion efficiency. For these reasons, tip-vortex cavitation represents an important design factor that should be considered for developing efficient ship propellers requiring low noise emissions and vibration levels. As such, tip-vortex cavitation necessitates a deeper understanding and more accurate modeling, particularly in relation to far-field noise emission.

According to Raestad (1996) and Bosschers (2007), the noise from tip-vortex cavitation is associated to the dynamic behaviour of the tip-vortex cavity. Bosschers (2009) proposed a theoretical dispersion relation to model

✉ Özge Başkan Perçin
obaskan@metu.edu.tr

[1] Department of Aerospace Engineering, Middle East Technical University, Ankara, Turkey

[2] Department of Maritime & Transport Technology, Faculty of Mechanical Engineering, Delft University of Technology, Delft, The Netherlands

[3] Department of Process & Energy, Faculty of Mechanical Engineering, Delft University of Technology, Delft, The Netherlands

Published online: 28 September 2024

the dynamics of the waves forming at the cavity-water interface of an isolated cavity. This theory was later confirmed from experiments of high-speed shadowgraphy on an isolated cavity originating from a hydrofoil tip (Pennings et al. 2015a). A characteristic tonal noise, identified as 'singing vortex' (Higuchi et al. 1989; Maines and Arndt 1997; Arndt 2002; Peng et al. 2017), is emitted when the resonance frequency of a standing wave predicted from the described dispersion relation is somehow excited (Arndt et al. 2015). Determining the resonance frequency of the volume-variation mode necessitates knowing the azimuthal velocity at the cavity interface as well as the cavity radius. For these reasons, Pennings et al. (2015b) measured the three-dimensional velocity field in a plane downstream of a cavitating tip vortex from a hydrofoil. The radial distribution of azimuthal velocity in close streamwise proximity of the tip was modelled through a Proctor vortex model. However, studying a cavitating tip vortex from a hydrofoil and not from a propeller represents a simplification of the problem.

In ship propellers, the source of excitation of the resonance frequency of tip-vortex cavities can be represented by the non-uniformity of the inflow conditions. This is caused by the turbulent wake field behind the hull. With the aim of mimicking the hull turbulent wake, Pennings et al. (2016) installed an array of plates upstream of the propeller hub. A louder noise was recorded in the case of turbulent wake inflow compared to a uniform non-turbulent inflow. The resonance frequency of the cavity dynamics could be predicted from the dominant frequency of the acoustic spectrum for the case of turbulent wake inflow. These experiments established a clear connection between the excitation of the cavity resonance frequency of the volume-variation mode, on one side, and the emission of far-field noise at that same frequency, on the other side. However, the authors could not measure the flow velocity around the tip-vortex cavity, which is a necessary quantity to determine the resonance frequency of the volume-variation mode. The flow field around the tip-vortex cavity also enter in the semi-empirical method proposed by Bosschers (2018a) for the estimate of hull-pressure fluctuations and underwater radiated noise. These examples show that characterizing the flow surrounding the tip-vortex cavity and its geometric properties is essential to predicting the noise emission from tip-vortex cavitation in propellers. Moreover, resolving the three-dimensional velocity field around a tip-vortex cavity enables the unveiling of the coherent structures responsible for the acoustic pressure fluctuations, thus better clarifying the mechanism by which the dynamic behaviour of a cavity translates to sound production. A first step towards expanding our understanding and predicting tip-vortex-cavitation noise is therefore to reconstruct the three components of the velocity vector field in the three-dimensional domain around the cavity. This can be done by means of tomographic particle image velocimetry (Tomo-PIV) (Elsinga et al. 2006).

Recently, tomography-based velocimetry techniques were applied to study cavitation inception and the flow around developed cavities. Zhao et al. (2023) investigated the near field of a non-cavitating tip vortex from an elliptical hydrofoil with Tomo-PIV. Three regions were identified, i.e. a vortex-attached region, a vortex-lifting region, and a vortex-detached region. From comparing these observations with previous studies, the extent of these regions and, more generally, the vortex evolution were hypothesized to be more sensitive to the trailing-edge geometry than to the flow conditions. Agarwal et al. (2023) applied tomographic particle tracking to non-cavitating quasi-streamwise vortices in the shear layer behind a backward-facing step. To gain a better insight into the mechanism leading to cavitation inception, the unsteady pressure field was reconstructed from spatial integration of the material acceleration. Using Tomo-PIV, Ye et al. (2023) unveiled the flow structures around a cavitating tip vortex in the wake of an elliptic hydrofoil. Two main cavitation modes were studied, namely the breathing and double-helical modes. The complexity and unsteadiness of the three-dimensional cavity increase noticeably with the decrease in cavitation number, which indicates that the cavity surface fluctuations contribute to the unsteadiness of the vortical structures.

The flow generated by the rotating movement of a marine propeller has also been the object of analysis. In the wake of a non-cavitating propeller, the flow structures associated to sound generation were experimentally investigated with Tomo-PIV by Felli et al. (2015b, 2015a). After applying Powell's acoustic analogy (Powell 1964), tip vortices were found to play a dominant role over hub vortex and trailing wake in the total noise emission. In the same Institute, i.e. at CNR-INM, optical techniques such as shadowgraphy and planar PIV were applied to study the dynamics of vortices in the wake of non-cavitating propellers at different working conditions (Felli and Falchi 2011; Felli et al. 2011; Felli and Falchi 2018).

The turbulent flow around a tip-vortex cavity in the wake of a rotating propeller has never been investigated with Tomo-PIV. The flow is both multi-phase and intermittent, and Tomo-PIV has been scarcely applied to this class of problems. A rare example is the study of Gawandalkar and Poelma (2022), who characterized the structure of a near-wall re-entrant jet in a cavitating venturi. Previously, volumetric measurement techniques had been applied around moving objects; see Adhikari and Longmire (2012, 2013), Van Hout et al. (2022), and Mendelson and Techet (2015, 2018), among others. Applying Tomo-PIV to the wake of a cavitating propeller brings with it some specific technical challenges. Firstly, the cavity obstructs the optical access to portions of the flow domain, which is expected to deteriorate the accuracy of the tomographic reconstruction. The cavity is a helix, which is long and thin, therefore geometrically different from the obstructing objects of previous experiments with Tomo-PIV. Also, the cavity extends outside the measured volume, and the effect that this has on the reconstruction accuracy is not yet fully understood. Secondly, the gaseous phase scatters spurious reflections. These reflections may significantly deteriorate the signal-to-noise ratio of the measurement if their intensity becomes conveniently larger than the light intensity originating from the particle images. Thirdly, the position, as well as the size of the cavity, vary over time; therefore, the masking of the obstructing object cannot be set a-priori, but it must be adjusted to the specific snapshot.

The aim of the present work is to measure the three-dimensional flows around tip-vortex cavities in the wake of a marine propeller using Tomo-PIV. We firstly explain how our experimental setup and methodology could successfully overcome the aforementioned technical challenges. Moreover, we demonstrate the benefits of masking the cavity when performing the reconstruction of the tomogram. Finally, we examine the obtained three-dimensional flows surrounding both non-cavitating and cavitating tip vortices. This is done by means of instantaneous visualizations as well as through statistical representations.

## 2 Experimental set-up and methodology

### 2.1 Experimental setup

The experiments are performed in the cavitation tunnel at the Delft University of Technology (see Fig. 1). A detailed description of the tunnel and the modifications made are given respectively in Foeth (2008) and in Zverkhovskyi (2014) and Pennings (2016). The tunnel has a test section with cross-section dimensions of $0.30 \times 0.30\,\mathrm{m}^2$ at the inlet and $0.30 \times 0.32$ $\mathrm{m}^2$ at the outlet so that a near-zero streamwise pressure gradient is achieved at the top and bottom walls of the test section (Pennings et al. 2015b). A right-handed two-blade marine propeller, which is provided by the Maritime Research Institute Netherlands (MARIN), is used as the experimental model, and it has a diameter $D$ of 0.15 m and a chord length $c$ of 0.054 m (at 70% radius location). The specific design of the blade facilitates the transformation of the leading-edge sheet cavity into the tip vortex. In the experiments, the rotational speed of the propeller $n$ and the free-stream velocity $U_\infty$ are set to 18.8 Hz and 1 m s$^{-1}$, respectively, resulting in an advanced ratio $J$ of 0.36, where the advanced ratio is defined as

$$J = \frac{U_\infty}{nD} \tag{1}$$

The pressure inside the water channel $p_\infty$ is varied systematically to investigate the influence of the cavitation number, defined as

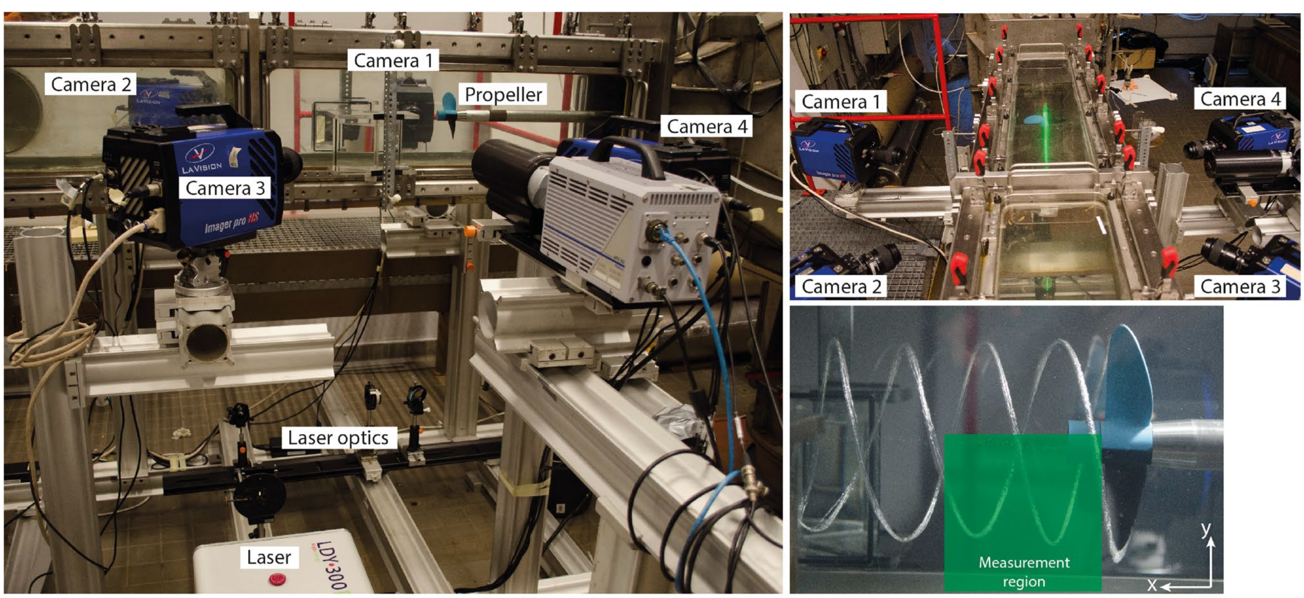


**Fig. 1** Overview of the experimental setup for the tomographic-PIV measurements. The setup comprises a marine propeller located in the test section of the cavitation tunnel, four cameras, a high-speed laser, and laser optics (left). The cameras are positioned on either side of the test section (top right). The measurement region with a volume of $100 \times 100 \times 10$ mm$^3$ is illuminated by a high-speed Nd: YLF laser (bottom right)

$$\sigma_n = \frac{(p_\infty - p_{\text{vap}})}{\frac{1}{2}\rho(nD)^2} \tag{2}$$

where $p_{\text{vap}}$ and $\rho$ are the vapour pressure and the density of water, respectively. The Reynolds number of the problem, i.e. Kempf's Reynolds number, is defined as

$$Re = \frac{c(U^2 + (0.7\pi nD)^2)^{0.5}}{\nu} \tag{3}$$

where $\nu$ is the kinematic viscosity of water and $U$ is the advance speed of the propeller. In the experiments, the propeller's axial position is fixed. Therefore, the propeller's advance speed $U$ is identical to the free-stream velocity of the flow, i.e. $U_\infty$, in the tunnel, which results in a Reynolds number of $3.1 \times 10^5$ in the experiments. The static pressure in the water channel is measured at a recording rate of 10 kHz using a digital absolute pressure sensor (Keller PAA33X) placed at the contraction exit.

The gas concentration in water contributes to the size of the cavity. Therefore, minimizing the amount of dissolved gas in the water before conducting the experiments is essential. The degasification procedure comprises four main steps: *i.*) the top part of the facility is partially filled with water so that the free surface of the water is enlarged, *ii.*) the tunnel and the vacuum pump are run simultaneously to remove gas bubbles in the water, *iii.*) the water level in the facility is increased to the level at which the experiments are performed while keeping the tunnel and the vacuum pump running and *iv.*) degassing is continued for a couple of hours and is terminated when there is no significant decrease in the dissolved gas concentration. Here, dissolved oxygen concentration *DO*, which is measured by an optical sensor (RDO Pro), is used as a measure of dissolved gas concentration in the water (Pennings et al. 2015b). The concentration is determined by taking water samples from the tunnel at the beginning and end of the experiments. The values reported in this paper are the averages of the samples' oxygen concentrations obtained before and after the measurements.

To assess the performance of the propeller under cavitating and non-cavitating flow conditions, the thrust and torque generated by the propeller are measured by two single-point load cells (Zemic L6D-C3) connected to the propeller shaft outside the tunnel. The torque caused by bearings/seals is also measured when the shaft is empty and then excluded from the total torque when calculating the net torque produced by the propeller. The capacities of the load cells used for measuring thrust and torque are 140 N and 45 N, respectively. The sampling frequency is 1.0 kHz, whereas the number of data points per case varies from 8000 to 175000.

## 2.2 Tomographic particle image velocimetry

The tomographic-PIV setup consists of four high-speed cameras (LaVision Imager Pro LX 16 M) placed on opposite sides of the test section (two cameras for each side, see Fig. 1). The cameras are equipped with Scheimpflug adapters and 105 mm Nikon objectives with a numerical aperture $f\# = 11$. Cameras 1 and 4 are placed at 10° off-axis angle, whereas Cameras 2 and 3 are at 50° off-axis angle. Two 45° prisms are used with Cameras 2 and 3 to reduce optical distortions. The measurement volume of $100 \times 100 \times 10$ mm$^3$ (width×height×depth) is illuminated by a high-speed Nd:YLF laser, where the laser enters the test section vertically upward through its bottom wall made of acrylic. The digital resolution is 20 pixels mm$^{-1}$, and the corresponding magnification factor is 0.22.

Spurious reflections and glare scattered by the gaseous phase complicate the application of the PIV technique in multi-phase flows. The experimental approach that is often adopted to overcome this issue is to combine the use of Rhodamine B particles (or particles of other materials with a coating of Rhodamine B), which absorb green light and emit orange light, with an optical filter that blocks any other sources of light at wavelengths shorter than orange light (Gawandalkar and Poelma 2022; Ye et al. 2023). In our experiments, a different approach is adopted. Illumination at relatively low energy density is obtained by expanding the laser beam through a cylindrical lens and a spherical lens in series. The access of light to the test section and the consequent size of the illumination volume are controlled by means of a pinhole positioned before the lenses and a fence in a sheet of carton paper through which the light passes. The latter is placed close to the bottom wall of the test section. Controlling the incoming light guarantees that the light intensity distribution is approximately uniform along the out-of-plane direction of the measurement volume, as the weaker peripheral region of the laser source is shielded by the pinhole and carton paper and does not contribute to the formation of the illumination volume. The aperture of the lenses is set in such a way that the intensity of the incoming light is high enough to have a high signal-to-noise ratio in the images. In this way, particle images are identifiable, and the illumination volume is contained within the depth of field. The flow is then seeded with 10 $\mu$m hollow glass particles with no silver coating (Sphericells). The average particle image density is approximately 0.04 particles per pixel (ppp).

Tomographic PIV images are captured at an image recording frequency of 640 Hz (double-frame, full resolution). The acquisition frequency was increased to 2.15 kHz after cropping the recordings and reducing the measurement volume size. Image acquisition, image preprocessing, volume calibration, self-calibration, reconstruction, three-dimensional cross-correlation-based interrogation, and universal outlier detection are performed in LaVision™ DaVis 8.3. Particle images are interrogated using windows of final size $40 \times 40 \times 40$ voxels for full-resolution cases and $32 \times 32 \times 32$ voxels for cropped cases, with an overlap factor of 75%, resulting in a vector spacing of 0.5 mm and 0.4 mm, respectively, in each direction. Void regions that may occur in the velocity field due to the intersection of masks covering the cavities in camera images (see Sect. 2.4) are filled up based on the median of the neighboring vectors.

### 2.3 Effect of cavities on tomographic reconstruction

In this section, the performance of the tomographic particle reconstruction is assessed when the view of the tracer particles is partially blocked by the presence of opaque objects. These opaque objects are located in between the measurement volume and the imaging optics and they resemble the helical cavity in our experiments. For brevity, we refer to them as 'cavities'; however, the results are generally applicable to all possible obstructions of the view. The presence of the cavity means that, locally within the measurement volume, the tracer particles are seen by a reduced number of cameras. The number of cameras that view a particular region will be referred to as camera cover. Presently, it is unclear how a locally-reduced camera cover affects the reconstruction accuracy of the MART reconstruction algorithm (where MART stands for multiplicative algebraic reconstruction technique). Recently, Wieneke and Rockstroh (2024) examined the blocking effect for Shake-the-box, but not for tomography. By means of simulated experiments, it will be shown that the local reconstruction quality does not degrade below the value expected for the camera cover. This is important because it validates our experimental approach and demonstrates that the local accuracy is predictable when using the local number of unobstructed views, i.e., the camera cover. Therefore, existing knowledge of the reconstruction performance (Elsinga et al. 2006, 2011) can be used to design experiments such that an acceptable level of accuracy is maintained throughout the volume.

The numerical simulations are essentially similar to those previously proposed by Elsinga et al. (2006, 2011). However, some parameter settings have been adjusted to mimic the present experiments, and the effect of cavities is included. Particles are distributed in a 2D, $2000 \times 200$ voxel slice of the volume, and they are imaged by four 1D arrays with 2000 pixels, representing a four-camera imaging system. The particle image diameter is 3 pixels, and the 1D particle image density is 0.12, which corresponds to a particle image density of 0.04 in 2D images (Elsinga et al. 2011). The particle image peak intensity is 80 counts. A coordinate system is defined in which $z$ is the volume depth coordinate and $x$ is the direction along the front of the volume slice. The viewing directions of the cameras with respect to the $z$-axis are -7, 40, -40, and 7 degrees for cameras 1–4, respectively. Cameras 1 and 2 are located at a large distance in the negative $z$-direction, while cameras 3 and 4 are at a large distance in the positive $z$-direction (Fig. 2).

A series of circular cavities with a diameter of 3 mm (corresponding to 60 voxels) are located on either side of the measurement volume, as shown in Fig. 2. This configuration represents a cross-section through the double helix cavity structure originating from a two-bladed propeller. The cavities block the view of the particles locally. The intensities in the corresponding pixels are set to a uniform value of 255 counts. Any other non-zero intensity could have been chosen because these pixels are not included in the MART reconstruction algorithm when masking is used (see below). Also, when these pixels are included in the MART iteration (no masking), the results do not sensitively depend on the chosen intensity level, provided it is non-zero. However, zero intensity leads the algorithm to believe that there are no particles in the corresponding part of the volume, which results in a significantly lower reconstruction accuracy.

Then, the volume intensity distribution is reconstructed from these images using the MART algorithm with 5 iterations. Reconstructions are performed with and without a masking procedure. The mask identifies the pixels with a blocked view of the volume and consequently skips these pixels in the MART iterations. As in our previous work, the accuracy of the reconstructed particle intensity distribution

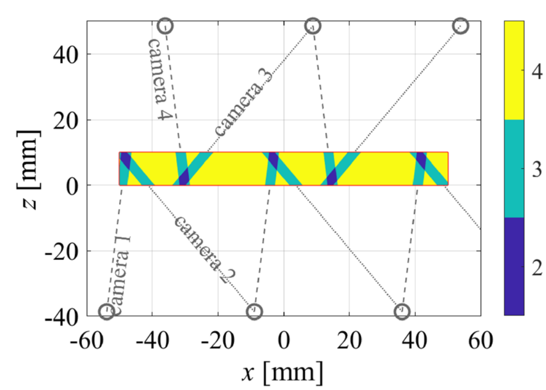


**Fig. 2** Layout of the simulated experiments. The 2D slice of the measurement volume is indicated by the red rectangle. The colour coding indicates the local camera cover, where the yellow regions are seen by all four cameras. Turquoise regions are seen by three cameras, while the view of the remaining camera is obstructed by the presence of a cavity in between the volume and the camera. Blue regions are seen by two cameras, while the view is blocked for the other two cameras. The cavity locations are marked by circles. The viewing directions of the cameras are indicated by grey dashed and dotted lines. They connect the cavities to the regions of reduced camera cover. Note that cameras 1,2 and 3,4 are placed on opposite sides of the volume as in our actual experiments. Cavities in the background are assumed to have no effect on the particle imaging

is quantified by means of the reconstruction quality factor, $Q_f$, which is defined as the correlation coefficient between the MART reconstructed intensity distribution and the so-called ideal reconstruction given by Gaussian intensity blobs at the actual particle positions (Elsinga et al. 2006), as in the following equation

$$Q_f = \frac{\sum_{x,z} E_1(x,z) E_0(x,z)}{\sqrt{\sum_{x,z} E_1^2(x,z) \cdot \sum_{x,z} E_0^2(x,z)}} \tag{4}$$

where $E_0$ is the ideal reconstruction and $E_1$ is the reconstructed particle intensity fields. The overall $Q_f$ is determined as well as a local $Q_f$, which considers only those regions with a specified camera cover in the correlation. Furthermore, 100 independent realizations (i.e. particle distributions) were used to evaluate $Q_f$.

The colours in Fig. 2 present the camera cover within the measurement volume. Several regions of 3-camera cover appear, which are elongated along the viewing directions of the different cameras. When these regions intersect, the camera cover reduces to 2. However, the size of the intersections is small and comparable to the cavity size. Importantly, there are no regions with single camera cover. The local reconstruction quality, $Q_f$, from the layout shown in Fig. 2 is presented in Fig. 3, both for the case with no masking and for the case with masking. The benefits produced by the masking procedure of the obstructions, which in this particular case are the cavities, can be appreciated. These benefits encompass the whole field of view, including regions characterized by a local camera cover equal to 4.

The precise values of local reconstruction quality for the different scenarios are presented in table 1. The first three rows of the table provide a baseline and show the effect of the number of cameras in case of clean images (i.e. no cavitation present). The bottom rows show the cavitation results without and with masking being applied. It is clear that without masking, the reconstruction quality is much lower

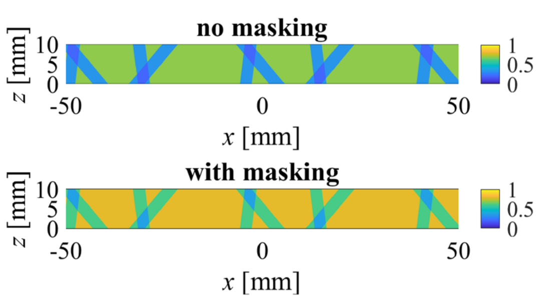


**Fig. 3** Local reconstruction quality, $Q_f$, for a 2D slice of a measurement volume as obtained from the layout of simulated experiments in Fig. 2, both for the case with no masking, top and for the case with masking, bottom

**Table 1** Local reconstruction quality, $Q_f$, in the regions with different camera cover. Cases without cavitation are included for reference

| | camera cover | | |
|---|---|---|---|
| case | 4 | 3 | 2 |
| 4 camera system, no cavitation | 0.81 | – | – |
| 3 camera system, no cavitation | – | 0.51 | – |
| 2 camera system, no cavitation | – | – | 0.28 |
| 4 camera system, with cavitation, no masking | 0.68 | 0.33 | 0.20 |
| 4 camera system, with cavitation, using masking | 0.79 | 0.60 | 0.37 |

than the baseline in all regions, even those that have a full 4-camera cover. However, when proper masking is applied, the reconstruction quality in the 4-camera cover regions is comparable to the expected performance for a 4-camera system in the case of clean images. A slight decrease in 0.02 is noticed in $Q_f$, which is not considered significant. The cavitation has virtually no effect in these regions. In the 2- and 3-camera cover regions, the reconstruction quality is higher than the baseline values when masking is used. This is attributed to the fact that lines of sight intersecting these regions also intersect with full camera cover regions, which are more accurately reconstructed. Finally, the overall $Q_f$ when using masking is 0.74, which is deemed sufficient for the present experiments. Therefore, masking should be used such that pixels with a blocked view of the measurement volume are skipped in the reconstruction.

In conclusion, the results of the simulated experiments reveal that applying masks to the cavities is beneficial to the reconstruction quality of the tomograms, with a consequent reduction in the measurement errors of the Tomo-PIV vector fields. It is worth noting that these considerations on the benefit of masking the cavity before performing the tomographic reconstruction are not circumscribed to multi-phase flow problems solely but can be extended to any Tomo-PIV experiment where the optical access to some regions of the flow is blocked by any optical obstructions. In the next section, the automated masking procedure that was applied to our Tomo-PIV images is discussed.

## 2.4 The automated masking procedure

Image pre-processing functions in Davis 8.3 are used to create masks for the flow regions blocked by cavities. The masking procedure consists of two main steps: *i.*) removal of particle images from the original images while retaining cavity images, and *ii.*) conversion of the cavity images into masks. In the first step, three functions are applied, i.e. 'strict sliding minimum', over a window of $7 \times 7$ pixels, 'subtract sliding average', over a window of $101 \times 101$ pixels, and 'subtract' a constant value of 10 counts. By means of these algorithms, raw images (Fig. 4, top) are converted into black and white images, in which white regions represent the identified cavities (Fig. 4, middle). Although the aforementioned functions are used to remove the particle images, they also tend to reduce the size of the cavity images. To compensate for this effect, the function 'dilatation' is also used on the binarized images. Then, the obtained images are converted into masks, which are applied to pre-processed images (Fig. 4, bottom). For the cases where the hub of the propeller is in the measurement volume, the hub images are covered by masks to increase the reconstruction quality, and hence, to decrease the errors in the vicinity of the hub. Since the hub is stationary, this process is not automated. Instead, fixed masks are used to cover hub images.

# 3 Results

## 3.1 Flow field characteristics

The experiments are performed at a range of cavitation numbers (Eq. 2). This physical parameter is varied by modifying the pressure inside the tunnel while keeping both the advance ratio (Eq. 1) and the Reynolds number (Eq. 3) constant. In the experiments, $J = 0.36$ and $Re = 3.1 \times 10^5$. The specific values of the free-stream velocity and rotational speed are respectively $U_\infty = 1\ \mathrm{m\ s^{-1}}$ and $n = 18.8$ Hz, with the latter equivalent to a blade passing frequency of 37.6 Hz for a two-blade propeller. In Fig. 5, a snapshot is shown of the three-dimensional time-resolved flow field obtained from Tomo-PIV of the wake of the propeller for a cavitation number of 6.64 (the flow is from left to right).

For the identification of the coherent structures of vorticity, the $Q$-criterion is adopted (Jeong and Hussain 1995), where the quantity $Q$ is defined as follows

$$Q = \frac{1}{2}(\lambda_1 + \lambda_2 + \lambda_3) \tag{5}$$

where $\lambda_1$, $\lambda_2$, $\lambda_3$ are the eigenvalues of $\mathbf{S}^2 + \mathbf{\Omega}^2$, with $\mathbf{S}$ and $\mathbf{\Omega}$ being respectively the symmetric and anti-symmetric parts of the velocity gradient tensor, $\nabla u$. Iso-surfaces of the quantity $Q$ are also presented in Fig. 5, which shows the three-dimensional vortical structures in the flow field. The contours at the backmost plane of the measurement volume represent the vertical component of the velocity ($y$-velocity). The types of coherent structures that can be identified in the volume are *i.*) the tip vortex, *ii.*) the hub vortex, and *iii.*) the secondary vortices around the tip vortex.

The hub of the propeller is located at the top-left corner of the measurement volume, and the vortical structure extending from the hub to the rightmost surface of the volume is the hub vortex. Two helical tip vortices emerge from the tips of the blades and intersect with the measurement volume at two regions. The intersection regions move in the flow direction as time progresses. Since the flow is periodic, we observe the periodic formation of the intersection regions at the inlet of the measurement volume. Secondary vortical

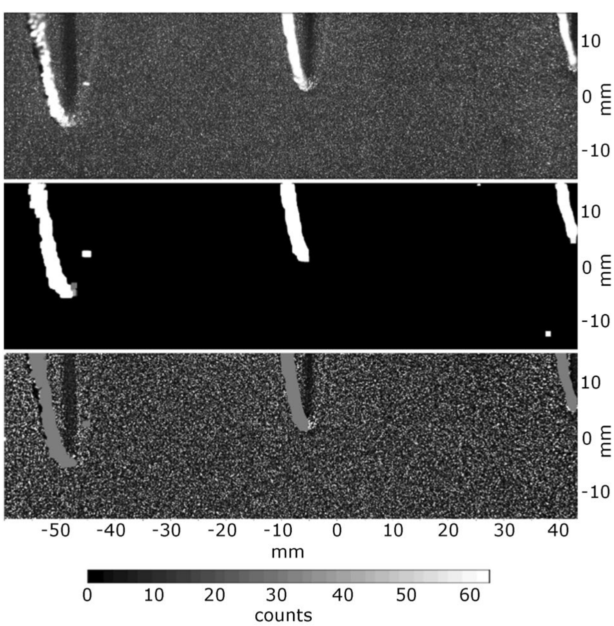


**Fig. 4** Masking and image pre-processing on a PIV image. Top: a raw PIV image. Middle: PIV image after the removal of the particle images. Bottom, the pre-processed PIV image after masking the cavities

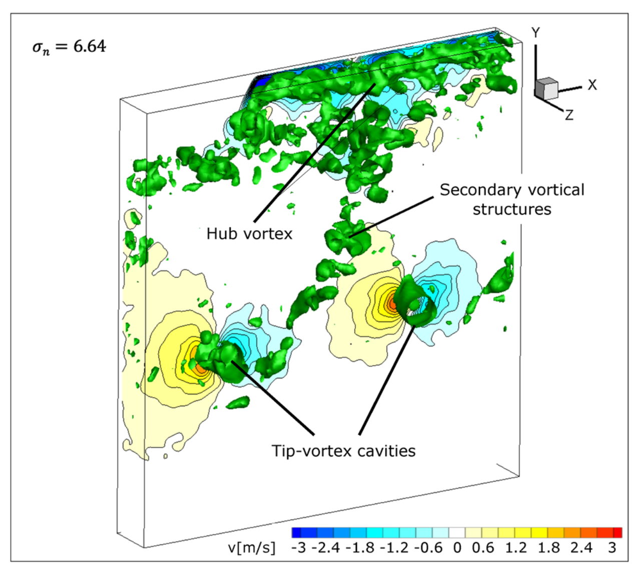


**Fig. 5** The three-dimensional flow field at the wake of the propeller at $Re = 3.1 \times 10^5$, $\sigma_n = 6.64$ and $J = 0.36$. The flow is in the positive x-direction. Green surfaces represent the iso-surfaces of the quantity $Q$ (Eq. 5, $Q = 3.0 \times 10^3\ \mathrm{s^{-2}}$), whereas the contours at the backmost plane of the measurement volume are the vertical velocity component $v$ ($y$-velocity). Dissolved oxygen concentration $DO = 3.5$ mg/L

structures are also present in the flow field, which extend from the hub vortex to the tip vortex. The top end of these structures is in interaction with the turbulent flow at the wake of the hub, and the bottom end encircles around the tip vortex. When the $y$-velocity distribution around the tip vortices is considered, the magnitude is the highest in the vicinity of the vortex, while it gets smaller as we get distant from the core of the vortex.

### 3.2 The effect of cavitation number on flow physics

The experimental results discussed in this section are obtained at four different tunnel pressure values, resulting in four different cavitation numbers, namely, $\sigma_n = 3.88, 6.37, 8.87, 14.0$. Fig. 6 shows the raw images taken during the experiments. In this figure, we see that at low cavitation numbers, cavities form at tip vortices and the size of the cavity decreases as the cavitation number increases. This is due to the fact that at low cavitation numbers, the tunnel pressure $p_\infty$ is closer to the vapour pressure $p_{vap}$ of water. The formation of cavities in the core of the vortices is observed when the local pressure drops below the vapour pressure of water, which is lower than the pressure inside the tunnel. In our experiments, cavitation occurs at cavitation numbers $\sigma_n = 3.88$ and 6.37. We also observe very small bubbles at high cavitation numbers, yet these bubbles appear temporarily.

The cases shown in Fig. 6 were investigated with Tomo-PIV, and the results are depicted in Fig. 7. In all four panels, the flow is in the positive $x$-direction, and green surfaces are iso-surfaces of $Q$ (Eq. 5). The contour plots at the backmost plane of the measurement volume represent the $y$-velocity. In the first case (Fig. 7-top left), a large cavity forms in the core of the tip vortex. The relatively low cavitation number is associated with the appearance of small and disordered coherent structures around the tip vortex. As the cavitation number increases, the small vortical flow structures gradually turn into a well-shaped secondary vortex around the tip vortex. An explanation for this observation is that at low cavitation numbers, the tip-vortex cavity induces pressure fluctuations within the surrounding flow, which breaks down the secondary vortical structure into smaller and dispersed structures. As the cavitation number increases, the cavity progressively disappears, and the cavitation-induced pressure fluctuations are gradually attenuated. This leads to the formation of an ordered secondary vortex around the tip vortex. The observation that the decrease in the cavitation number leads to an enhanced fragmentation and complexity of the flow structures surrounding the tip vortex or the cavity is consistent with the recent experimental work of Ye et al. (2023) on a fixed foil.

#### 3.2.1 Velocity profile across the tip vortex

Up until here, the observed modifications of the flow structures surrounding the tip vortices have been based solely on instantaneous snapshots of isosurfaces of $Q$ (see Fig. 6). In order to give statistical support to these observations, the velocity fluctuations in the close proximity to cavitating and non-cavitating tip vortices are analyzed. Only the mid-plane of the different three-dimensional velocity fields is considered in the analysis. It is worth mentioning that the vortices are not perfectly perpendicular to the mid-plane of the measurement volume, even though they were assumed to be perpendicular for simplicity in our analyses. First, the component associated with the rigid rotation of the tip vortices in the mid-plane of the domain is determined through the modified Rortex identification method by Liu and Liu (2019), which is based on the method introduced and described comprehensively in the studies of Tian et al. (2018) and Liu et al. (2018). This method is particularly suitable to our problem, in that it is Galilean invariant, and, therefore, it does not require knowing a-priori the advection velocity of the vortex itself. Then, the geometric center of each Rortex patch belonging to tip vortices is set as the center of the vortex in the analyses. After finding the center of the vortices in the flow field, the velocity profile around each vortex is obtained by defining a horizontal line passing through the geometric center of each vortex and extracting the y-component of the velocity vectors along this line. A local horizontal coordinate $r$ is then defined in such a way that $r = 0$ always

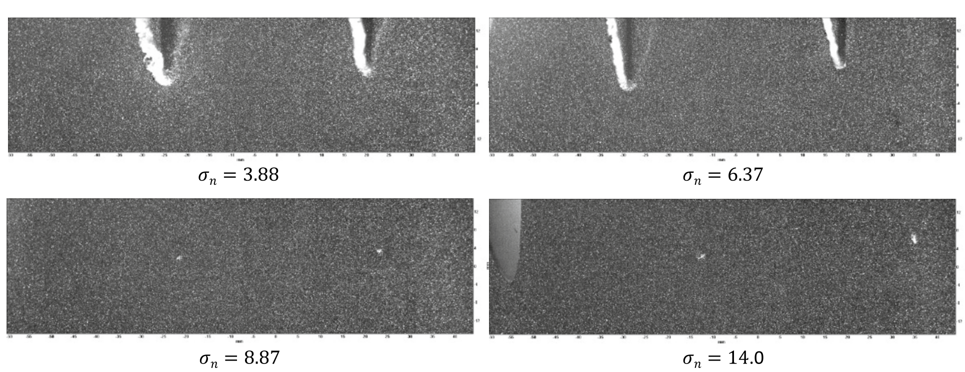


**Fig. 6** The effect of cavitation number on tip-vortex cavitation. At low cavitation numbers, cavitation occurs. As the cavitation number increases, the size of the cavity decreases, and only bubbles appear

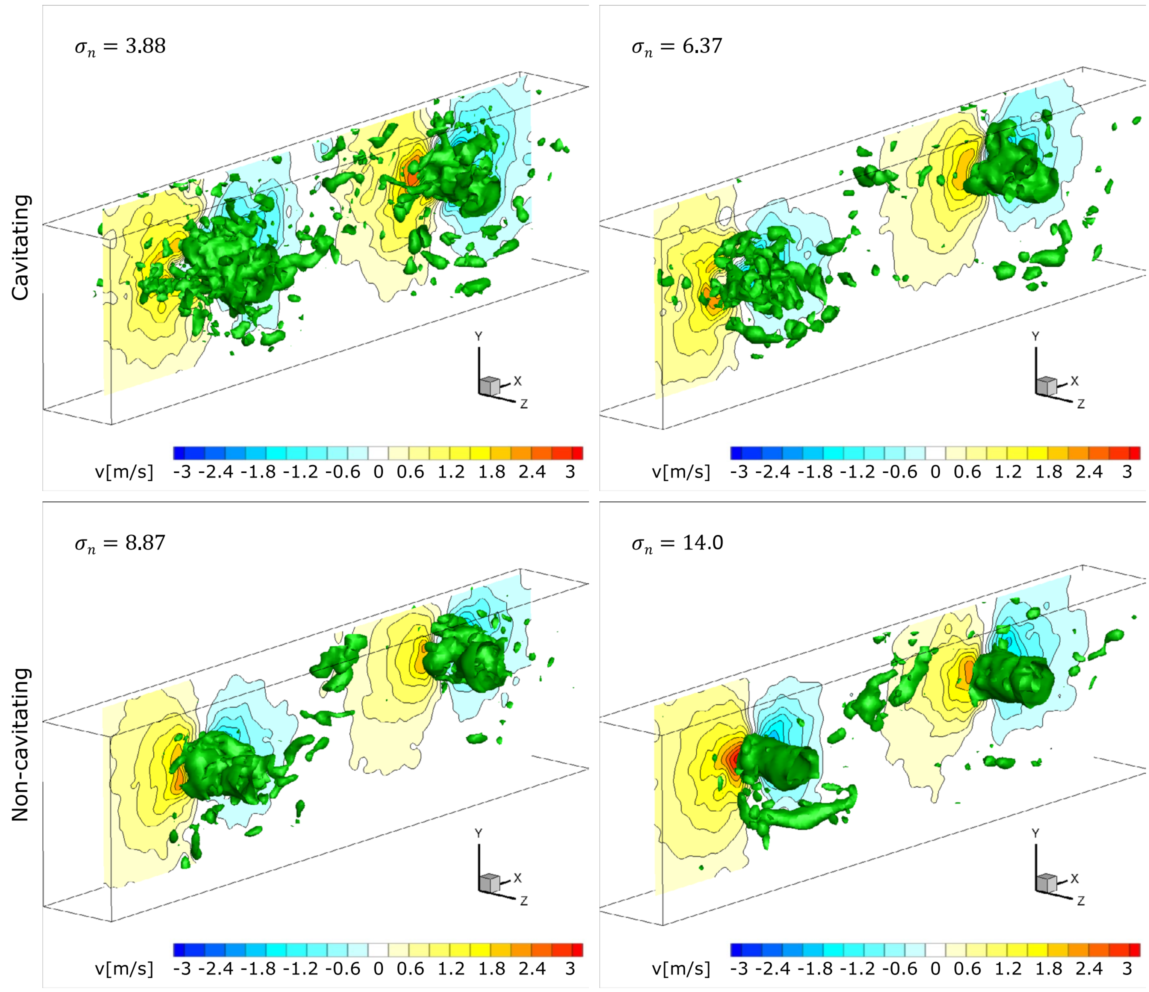


**Fig. 7** The effect of cavitation number on the flow field characteristics. Experiments were performed at constant Reynolds number and advance ratio, respectively $Re = 3.1 \times 10^5$ and $J = 0.36$. The cavitation number was varied as $\sigma_n = 3.88, 6.37, 8.87, 14.0$. The flow is in the positive x-direction. Green surfaces represent the iso-surfaces of the $Q$-criterion ($Q = 2.5 \times 10^4\ s^{-2}$), whereas the contours at the backmost plane of the measurement volume are the vertical velocity component $v$ ($y$-velocity). Dissolved oxygen concentration $DO = 2.9$ mg/L

coincides with the geometric center of each vortex. A statistical analysis is performed on the velocity profiles across the vortices obtained from 230 vector fields to determine the mean velocity profiles and the root mean square of the fluctuations from the mean velocity profiles. The results are presented in Fig. 8 for different cavitation numbers. Here, the black lines represent the mean velocity profile across the vortices in the flow field, and the gray shaded areas are the root mean square (r.m.s.) of the velocity fluctuations. The profiles of mean vertical velocities reflect the characteristic distribution of the azimuthal velocity around a vortex. Some small differences exist between these mean velocity profiles. These differences are most probably caused by mild variations in the relative position of the different vortices with respect to the measurement volume. The distribution of the velocity r.m.s., however, appears to depend on cavitation number, which confirms our previous observations. Consistent to what is observed in Fig. 6, larger values of r.m.s. velocity fluctuations are obtained for decreasing cavitation numbers. A remarkable difference exists when comparing non-cavitating cases with cavitating ones.

These observations can be corroborated when looking at Fig. 9, where the r.m.s. of the velocity fluctuations is presented for different cavitation numbers, with the aim of facilitating the comparison. Gray markers are associated with cavitating cases, while black markers are associated with non-cavitating ones. Even though close to the vortex core, the largest values of $v'_{\mathrm{rms}}$ are obtained for $\sigma_n = 6.37$, on the lateral branches, the largest variance manifests for $\sigma_n = 3.88$. At these radial positions, the difference between cavitating and non-cavitating cases is very large, thus supporting what is observed from isosurfaces of $Q$. Overall,

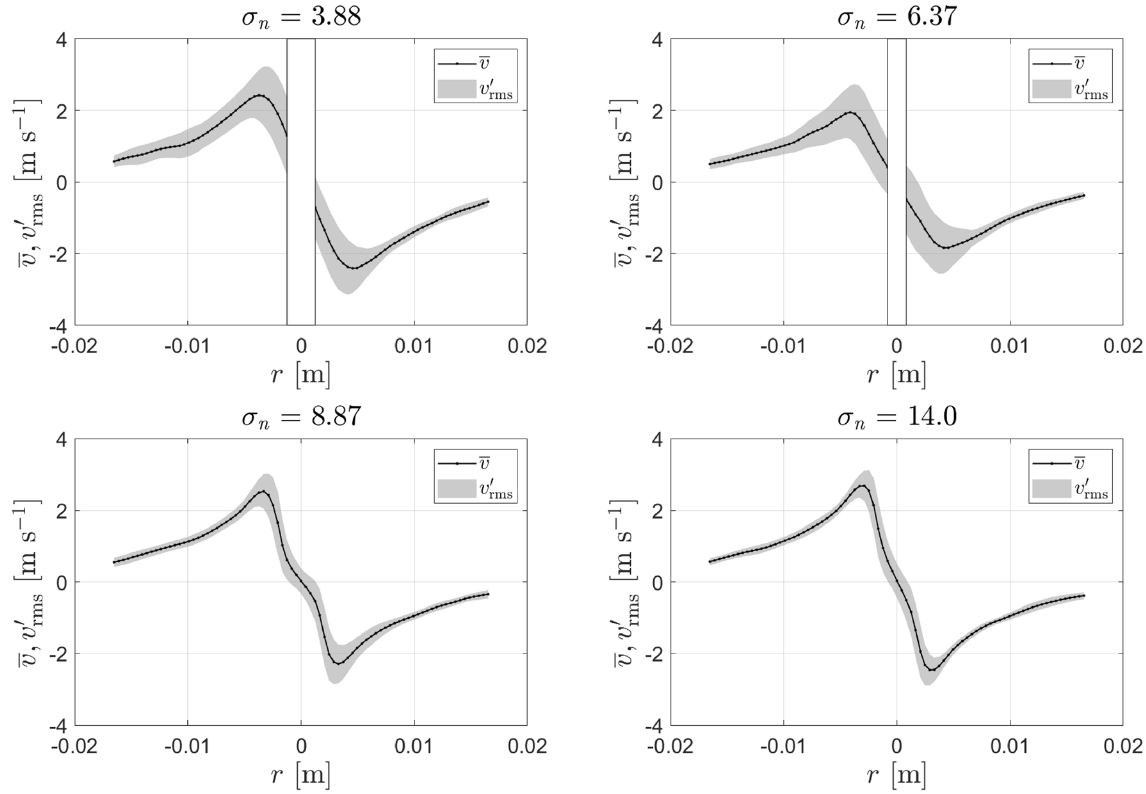


**Fig. 8** Statistics of the vertical velocity profiles along local horizontal lines intersecting the centers of the tip vortices for different cavitation numbers $\sigma_n$. $\overline{v}$ denotes the ensemble averages of the velocity profiles (black circles), whereas $v'_{\mathrm{rms}}$ stands for the r.m.s. of the fluctuations of the vertical velocities (gray regions). $r$ represents a local horizontal abscissa having its origin at the centers of each vortex. The cavitation numbers under investigation are 3.88 (top-left), 6.37 (top-right), 8.87 (bottom-left), and 14.0 (bottom-right). For $\sigma_n = 3.88$ and $\sigma_n = 6.37$, the two vertical lines delimiting the white regions around $r = 0$ identify the radial extent of the tip-vortex cavities

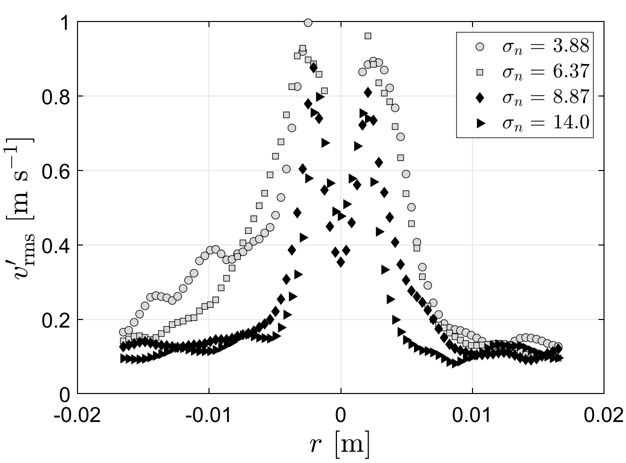


**Fig. 9** Root mean square of the fluctuations of the vertical velocities along local horizontal lines intersecting the centers of the tip vortices for different cavitation numbers $\sigma_n$. $r$ represents a local horizontal abscissa having its origin at the center of each vortex. The cavitation numbers under investigation are reported in the legend in the top right

lowering the cavitation number leads to stronger velocity fluctuations around the tip vortices. A marked jump in the variance occurs when moving from non-cavitating to cavitating tip vortices.

### 3.2.2 Force and torque measurements

We conclude the section on the results by presenting the experimental measurements of the thrust and torque coefficients for different cavitation numbers. The thrust and torque coefficients are respectively defined as

$$K_T = \frac{T}{n^2 D^4 \rho} \tag{6}$$

and

$$K_Q = \frac{Q}{n^2 D^5 \rho}, \tag{7}$$

where $T$ and $Q$ are the thrust force and the torque, respectively. Thrust and torque coefficients are shown in Fig. 10 for cavitation numbers varying from 3.00 to 24.5, where

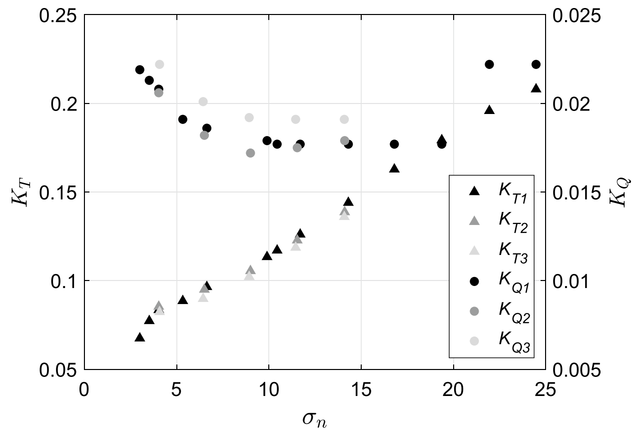


**Fig. 10** The experimental relationship between thrust and torque coefficients, respectively $K_T$ and $K_Q$, and cavitation number $\sigma_n$. The triangles denote the thrust coefficients, whereas the circles stand for the torque coefficients. The different shades of gray of the filled symbols represent data obtained from multiple runs conducted at different times

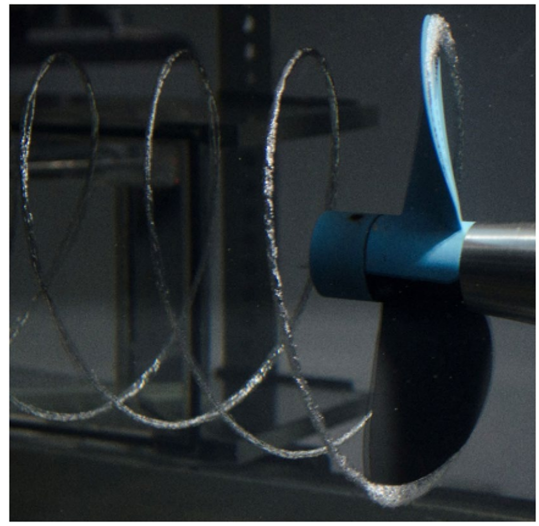

**Fig. 11** Photo showing the cavitating propeller and the developing tip-vortex cavities in its wake, for the case $\sigma_n = 3.88$. On the blade surface of the top blade, a vapour cavity can be observed, which is expected to cause a drop in the propeller performance

triangles denote the thrust coefficients and circles the torque coefficients. The different shades of gray of the symbols represent different experiments conducted on different days, which are aimed at assessing the repeatability of the experimental results. The uncertainties associated with random error for these values of thrust and torque coefficients are estimated to be always smaller than 0.3%.

It can be observed that the values of the thrust coefficients decline for decreasing cavitation numbers, with the trend being linear over most of the range. However, when the cavitation number is lower than $\sigma_n \approx 5$, a different trend slope manifests, with the value of the thrust coefficient decreasing more rapidly. It is important to notice that no discontinuity is observed in the range $6.37 < \sigma_n < 8.87$, i.e., at the onset of tip-vortex cavitation, see Fig. 6. The observed change in the slope of $\sigma_n - K_T$ occurs in fact at lower cavitation numbers, i.e. at $\sigma_n < 5$. This is a consequence of a cavity volume forming near the blade surface, which modifies the pressure distribution around the blade, thus deteriorating the propeller performance. The formation of such cavity at the blade, possibly sheet cavitation in its early stage, can be observed in Fig. 11 for the case $\sigma_n = 3.88$. Similar observations can be made when commenting on the behavior of the torque coefficients. The torque coefficients exhibit a marked growth when the cavitation number decreases below $\sigma_n \approx 5$, which can again be associated with the formation of cavities at the blade surface. For cavitation numbers raising beyond $\sigma_n \approx 5$, $K_Q$ remains nearly constant. The values of $K_T$ for $\sigma_n = 22.0, 24.5$ seem to be outliers. This is, however, difficult to state with certainty because only one test has been conducted for each of these two cases. Therefore, to summarize, decreasing the cavitation number below a threshold value of $\sigma \approx 5$ produces a drop in the thrust coefficients as well as a growth of the torque coefficients. This threshold value of the cavitation number is associated with the formation of a cavity at the blade surface, possibly early-stage sheet cavitation, which tends to appear at lower cavitation numbers than tip-vortex cavitation. Moreover, the onset of tip-vortex cavitation, occurring at $6.37 < \sigma_n < 8.87$, does not lead to any discontinuities in the trends $\sigma_n - K_T$ and $\sigma_n - K_Q$. If we generally comment on the repeatability of the results, the measurements of the thrust coefficients are very repeatable, while more scattering is observed on the torque coefficients. However, despite the lower repeatability of the latter data, the general relationship between the torque coefficients and the cavitation number is well captured from each of the three runs.

## 4 Conclusions and future work

In the present work, time-resolved tomographic particle image velocimetry was applied for the first time to investigate the turbulent flow around a tip-vortex cavity in the wake of a ship propeller. The Reynolds number and the advance ratio were kept constant throughout the experimental campaign, while the cavitation number was modified from $\sigma_n = 3.88$ to $\sigma_n = 14.0$ by varying the pressure inside the cavitation tunnel. A factor hampering the accurate reconstruction of the three-dimensional vector fields in this class of problems is represented by the optical obstruction of the cavity, which reduces the number of cameras that view a particular region of the flow, referred to as camera cover.

Regions presenting low values of camera cover are typically characterized by a low quality of the tomographic reconstruction. However, it was demonstrated that masking the cavity improves the reconstruction quality considerably, and, not only in regions where the camera cover is 2 or 3, but also in regions to which all the 4 cameras have optical access.

After having derived the three-dimensional velocity vector fields, the vortices in the wake of the cavitating propeller were identified using the $Q$-criterion. Three coherent structures of vorticity were observed, i.e., the tip vortex, the hub vortex, and the secondary vortices. A vapour cavity appeared at $\sigma_n = 3.88$ and $\sigma_n = 6.37$, while the cases $\sigma_n = 8.87$ and $\sigma_n = 14.0$ were considered non-cavitating ones. The tip vortex and the secondary vortical structures were found to be highly sensitive to the cavitation number. The iso-surfaces of $Q$ identifying the tip vortices were increasingly more corrugated as the cavitation number was reduced. Moreover, the secondary vortical structures surrounding the tip vortex were broken down into gradually smaller and chaotically organized structures for diminishing cavitation numbers. A possible explanation for these observations is that the appearance of vapour pockets at the tip-vortex core induces pressure fluctuations that fragment the coherent secondary vortices into smaller motions. This effect is accentuated by the decrease in the cavitation number, which leads to progressively larger cavities. At the largest cavitation number, $\sigma_n = 14.0$, well-shaped secondary structures were observed, oriented almost perpendicularly with respect to the tip vortex. Statistical support was gained from calculating the r.m.s. of the vertical velocity fluctuations on horizontal lines intersecting the vortex cores. Larger values were obtained when lowering the cavitation number. Moving from $\sigma_n = 8.87$ to $\sigma_n = 6.37$ determine a remarkable growth of the r.m.s. of the vertical velocity fluctuations, which could be attributed to the onset of tip-vortex cavitation.

The thrust and torque coefficients were also measured on the same propeller for different cavitation numbers. It was found that the thrust coefficient decreases monotonically for lower cavitation numbers. When the cavitation number drops below the range $6.37 < \sigma_n < 8.87$, at which tip-vortex cavitation appears, the curve $\sigma_n - K_T$ continues to follow the same trend. However, below $\sigma_n \approx 5$, the descent becomes much steeper, which is probably associated with the formation of cavity volumes on the blade surface having a negative impact on the pressure distribution and, thus, on the thrust. Similar observations can be made when looking at the torque coefficient, which remains approximately constant until $\sigma_n \approx 5$, while for $\sigma_n < 5$ it presents an increasing trend.

To summarize, the study showed that the three-velocity components in the three-dimensional domain surrounding a tip-vortex cavity from a marine propeller can be measured, which has never been done before. From analyzing the obtained velocity vector fields, we could observe that a cavitating tip vortex strongly enhances the turbulence levels in the surrounding flow compared to a non-cavitating tip vortex. The unique dataset that was generated will be used to validate numerical simulations of the flow behind cavitating marine propellers. In future work, a model for the flow velocity around the tip-vortex cavity will be derived. Moreover, the pressure field around the cavity will be reconstructed from the time-resolved velocity fields. Indirect methodologies, such as acoustic analogies, will be applied to quantify the far-field noise, which will open up opportunities to better understand the mechanism for noise generation.

**Acknowledgements** This research was partially funded by the Dutch Research Council (NWO), The Netherlands, as part of the NOISOURCE, The Netherlands project (ALWTW.2016.008), and by the Dutch Ministry of Economic Affairs, The Netherlands.

## References


Adhikari D, Longmire EK (2012) Visual hull method for tomographic PIV measurement of flow around moving objects. Exp Fluids 53:943–964

Adhikari D, Longmire EK (2013) Infrared tomographic PIV and 3D motion tracking system applied to aquatic predator-prey interaction. Meas Sci Technol 24:024011

Agarwal K, Ram O, Lu Y, Katz J (2023) On the pressure field, nuclei dynamics and their relation to cavitation inception in a turbulent shear layer. J Fluid Mech 966:A31

Arndt REA (1981) Cavitation in fluid machinery and hydraulic structures. Annu Rev Fluid Mech 13:273–328

Arndt REA (2002) Cavitation in vortical flows. Annu Rev Fluid Mech 34:143–175

Arndt REA, Pennings PC, Bosschers J, van Terwisga TJC (2015) The singing vortex. Interface Focus 5:20150025

Bosschers J (2007) Broadband hull pressure fluctuations and cavitating vortices. In: Proceedings of the ship noise and vibration conference, September 2007, London, UK

Bosschers J (2009) Investigation of hull pressure fluctuations generated by cavitating vortices. In: First international symposium on marine propulsors, June 2009, Trondheim, Norway

Bosschers J (2018) An analytical and semi-empirical model for the viscous flow around a vortex cavity. Int J Multiph Flow 105:122–133

Bosschers J (2018b) Propeller tip-vortex cavitation and its broadband noise. PhD thesis, University of Twente

Carlton J (2018) Marine Propellers and Propulsion, 4th edn. Elsevier, Amsterdam

Duarte CM, Chapuis L, Collin SP, Costa DP, Devassy RP, Eguiluz VM, Erbe C, Gordon TAC, Halpern BS, Harding HR, Havlik MN, Meekan M, Merchant ND, Miksis-Olds JL, Parsons M, Predragovic M, Radford AN, Radford CA, Simpson SD, Slabbekoorn H, Staaterman E, van Opzeeland IC, Winderen J, Zhang X, Juanes F (2021) The soundscape of the anthropocene ocean. Science 371

Elsinga GE, Scarano F, Wieneke B, van Oudheusden BW (2006) Tomographic particle image velocimetry. Exp Fluids 41:514–539

Elsinga GE, Westerweel J, Scarano F, Novara M (2011) On the velocity of ghost particles and the bias errors in Tomographic-PIV. Exp Fluids 50:825–838

Felli M, Falchi M (2011) Propeller tip and hub vortex dynamics in the interaction with a rudder. Exp Fluids 51:1385–1402

Felli M, Falchi M (2018) Propeller wake evolution mechanisms in oblique flow conditions. J Fluid Mech 845:520–559

Felli M, Camussi R, Di Felice F (2011) Mechanisms of evolution of the propeller wake in the transition and far fields. J Fluid Mech 682:5–53
Felli M, Falchi M, Dubbioso G (2015) Experimental approaches for the diagnostics of hydroacoustic problems in naval propulsion. Ocean Eng 106:1–19
Felli M, Falchi M, Dubbioso G (2015) Tomographic-PIV survey of the near-field hydrodynamic and hydroacoustic characteristics of a marine propeller. J Ship Res 59(4):201–208
Foeth EJ (2008) The structure of three-dimensional sheet cavitation. PhD thesis, Delft University of Technology
Gawandalkar U, Poelma C (2022) The structure of near-wall re-entrant flow and its influence on cloud cavitation instability. Exp Fluids 63:77
Higuchi H, Arndt REA, Rogers MF (1989) Characteristics of tip vortex cavitation noise. J Fluids Eng 111:495–501
Hildebrand J (2009) Anthropogenic and natural sources of ambient noise in the ocean. Mar Ecol Prog Ser 395:5–20
IMO (2014) Guidelines for the reduction of underwater noise from commercial shipping to address adverse impacts on marine life. Tech. Rep. MEPC.1/Circ.833, International Maritime Organization, London, UK
Jeong J, Hussain F (1995) On the identification of a vortex. J Fluid Mech 285:69–94
Jones N (2009) Ocean uproar: saving marine life from a barrage of noise. Nature 568:158–161
Liu C, Gao Y, Tian S, Dong X (2018) Rortex-a new vortex vector definition and vorticity tensor and vector decompositions. Phys Fluids 30(3):035103
Liu J, Liu C (2019) Modified normalized Rortex/vortex identification method. Phys Fluids 31(6):061704
Maines B, Arndt REA (1997) The case of the singing vortex. J Fluids Eng 119:271–276
Mendelson L, Techet AH (2015) Quantitative wake analysis of a freely swimming fish using 3D synthetic aperture PIV. Exp Fluids 56:135
Mendelson L, Techet AH (2018) Multi-camera volumetric PIV for the study of jumping fish. Exp Fluids 59:10
Peng X, Wang B, Li H, Xu L, Song M (2017) Generation of abnormal acoustic noise: singing of a cavitating tip vortex. Phys Rev Fluids 2:053602
Pennings PC (2016) Dynamics of vortex cavitation. PhD thesis, Delft University of Technology
Pennings PC, Bosschers J, Westerweel J, van Terwisga TJC (2015) Dynamics of isolated vortex cavitation. J Fluid Mech 778:288–313
Pennings PC, Westerweel J, van Terwisga TJC (2015b) Flow field measurement around vortex cavitation. Exp Fluids 56:206
Pennings PC, Westerweel J, van Terwisga TJC (2016) Cavitation tunnel analysis of radiated sound from the resonance of a propeller tip vortex cavity. Int J Multiph Flow 83:1–11
Powell A (1964) Theory of vortex sound. J Acoust Soc Am 36:177–195
Raestad AE (1996) Tip vortex index—an engineering approach to propeller noise prediction. TNA
Tian S, Gao Y, Dong X, Liu C (2018) Definitions of vortex vector and vortex. J Fluid Mech 849:312–339
Van Hout R, Hershkovitz A, Elsinga GE, Westerweel J (2022) Combined three-dimensional flow field measurements and motion tracking of freely moving spheres in a turbulent boundary layer. J Fluid Mech 944:A12
Wieneke B, Rockstroh T (2024) Lagrangian particle tracking in the presence of obstructing objects. Meas Sci Technol 35(5):055303
Ye Q, Wang Y, Shao X (2023) Dynamics of cavitating tip vortex. J Fluid Mech 967:A30
Zhao H, Tu H, She W, Gao Q, Cao Y, Peng X, Shao X (2023) An experimental study on near-field tip vortex of an elliptical hydrofoil using tomographic particle image velocimetry. Exp Fluids 64:1–17
Zverkhovskyi O (2014) Ship drag reduction by air cavities. PhD thesis, Delft University of Technology

**Publisher's Note** Springer Nature remains neutral with regard to jurisdictional claims in published maps and institutional affiliations.

Springer Nature or its licensor (e.g. a society or other partner) holds exclusive rights to this article under a publishing agreement with the author(s) or other rightsholder(s); author self-archiving of the accepted manuscript version of this article is solely governed by the terms of such publishing agreement and applicable law.